Maximum-Power-per-Ampere Variable Frequency Modulation for Dual Active Bridge Converters in Battery Balancing Application

Weizhong Wang and Matthias Preindl, *Senior Member, IEEE*

***Abstract*—Varying the operating frequency helps dual-active bridge topologies increase the system efficiency since the soft-switching is regained at low-load condition. This paper proposes a conduction-loss-based variable frequency modulation (VFM) that decouples the phase shift from the frequency control that conventional VFM applies. The power losses for the shared-bus battery balancing topology are elaborated as switching frequency varies. The results show that increasing the operating frequency within the reasonable boundaries can benefit not only the switching loss but also the conduction losses. The switching loss is nearly constant, whereas the conduction losses decrease significantly. A factor of output power and transformer current, namely power-per-ampere, is derived as a function of operating conditions and phase shift independent of switching frequency. The operating setpoints are selected to minimize the factor using both online and offline optimizations. The proposed control strategy outperforms constant frequency modulation by up to 30% below 30% rated power. Furthermore, compared with conventional VFM, the proposed method improves the efficiency of the system under test by 1.5% below 50% normalized power, with significantly less computational resources needed.**

***Index Terms*—Battery balancing, Conduction loss, Dual-active bridge, Variable frequency modulation**

I. Introduction

IMBALANCE in large battery packs for electrical vehicles (EVs) viciously affects the vehicle performance and durance. Intelligent and high-efficient balancing approaches are desired. Compared with dissipative balancing strategy, redistributive is faster and more efficient but requires individual DC/DC converters [1]. The converters based on dual-active bridge (DAB) topology are the most promising technology that can achieve desired merits for battery balancing [2], [3].

DAB-based converters with the phase-shift modulation inherently equip with the soft-switching capability to increase the efficiency of the converter [4]–[6]. However, the converters are commonly designed for their nominal load conditions under zero-voltage switching (ZVS) operation at a constant switching frequency, which is known as constant frequency modulation (CFM). When the converter is operating with the low power load, the soft-switching capability can be compromised in addition to the increased conduction loss due to elevated root mean squired (RMS) currents through the components [7]. There are advanced phase shift modulations, such as dual phase shift modulation, that could potentially decrease the RMS current [8]. However, these modulations only apply to full-bridge topologies as they rely on injecting phase shift between two adjunct half bridges, which is unachievable for dual-active half bridge (DAHB) system.

Instead of operating at constant switching frequency, the switching frequency is adjusted at low-load conditions to maintain soft-switching capability and it continuously tunes the switching frequency when load increases. This is so-called variable frequency modulation (VFM). The optimized VFM [9] is achieved through comprehensively analyzing each component and concluding on an optimal operating-frequency map to minimize the loss of the entire system. The repetitive modeling and time-consuming surveying of the components that generate the major losses, such as power MOSFETs and inductors/transformers, are required. Another strategy is oriented to enable the ZVS at its minimal energy, so-called critical soft switching [10], [11]. In addition, the ZVS current is significantly dynamic and highly dependent on the half-bridge input voltages, as shown in Fig. 2, which are often assumed to be identical for most of the applications [4], [5], [12], i.e. $V_1 = V_2$. However, the additional freedom on the half-bridge input voltages in the battery-balancing auxiliary power module (BB-APM) application [2], [3] leads to a 4D-look-up table (LUT) of a function of $[V_1, V_2, d, f_s]$ instead of $[V_{in}, d, f_s]$, which makes storing and extracting the desired operating points less efficient on the embedded systems. In addition, the conduction loss is not considered to minimize, while it has been found that the conduction loss is dominant [13].

This study analyzes the conditions to enable ZVS at low load conditions, and proposes a conduction-loss criteria and a control law of VFM to drive the half-bridge based topologies, e.g. DAB, half-full bridge (HFB) and DAHB, to their pseudo-optimal condition in order to increase the system efficiency at low-load conditions without complicating the implementation on a microcontroller. It is a general approach to increase the efficiency and simplify the control for DAB based topology with phase-shift control at low-load conditions. However, in this study, it is applied to the BB-APM to increase the efficiency of high voltage (HV) battery pack to low-voltage

Manuscript received September, 2020, revised January 2021, April 2021, and May 2021; accepted Jun 10, 2021.
Weizhong Wang and Matthias Preindl are with the Electrical Engineering Department, Columbia University, New York, 10025, USA. (email: matthias.preindl@columbia.edu)

(LV) system when auxiliary loads, such as air conditioner and entertainment systems, are not activated. Input voltages v_1 and v_2 indicate two cells' voltages for one BB-APM link [3] in this study.

The paper is organized as follows: Section II analyzes the conditions the DAB-based topologies need to satisfy in order to guarantee all switches running under the ZVS; the tendencies of the power losses as the operating frequency increases are explained in Section III; the power per ampere (PPA) criteria and maximum power per ampere (MPPA) optimization are introduced in Sections IV and V; based on MPPA, the improved MPPA-based VFM is discussed and validated in Sections VI and VII, respectively; lastly, the paper is concluded in Section VIII.

II. Conventional Soft-Switching on DAB-Based Topologies

A. System parameters

The system under consideration is a BB-APM that powers the LV auxiliary power module by converting two HV battery modules and balances out the HV battery modules with a series of BB-APM and intelligent central controller [3], as shown in Fig. 1. The isolated DC-DC converter is illustrated in Fig. 2. The DAHB topology along with the loosely-coupled transformer model will be used for the derivation of the ZVS criteria for both primary and secondary switches. In addition, the conduction loss model will be dependent on the transformer model.

As the LV power consumption varies based on LV system usage, e.g. air conditioning and heated seats, output power requirement of BB-APM will change correspondingly. Therefore, the system is desired to operate at high efficiency regardless of output power. The system specs are detailed in Table I.

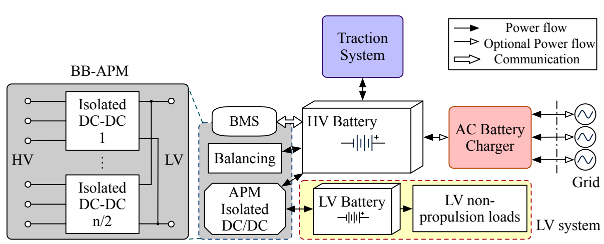

Fig. 1: BB-APM in EV application

TABLE I: The specifications of a single BB-APM

Parameter	Range
Input voltages V_1 and V_2	3.3 - 4.2 V
LV/output voltage V_{LV}	12-14 V
Output power P_o	0 - 50 W
Switching frequency f_s	100 - 1000 kHz

The transformer is modeled considering imperfect coupling, i.e. coreless transformers. The primary- and secondary-side self inductances are denoted as L_p and L_s, respectively. The turns ratio is defined as a, and transformer coupling coefficient is k. The coupling coefficient is as high as 0.99 for transformer with magnetic cores, but it can be low if the core is removed [14]. Therefore, the coupling coefficient is considered in the modeling.

Note that the superscript prime indicates the variable is referred from secondary side of the transformer to primary side unless specified otherwise, e.g. the terminal voltage on secondary side of the transformer v_o is referred to primary side as v_o'.

In the equivalent circuit for the transformer, only parasitic inductances are considered, whereas the intra- and inter- winding capacitances are ignored since those capacitances mainly determine the transient behavior of the switching instance instead of circuit operation.

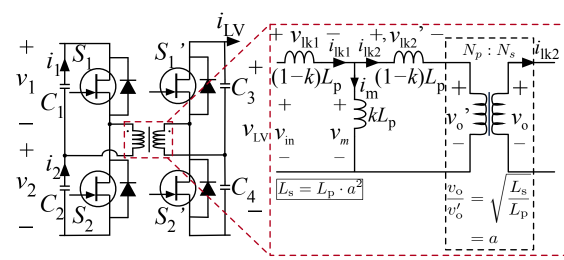

Fig. 2: The DAHB topology with generalized transformer model considering imperfect coupling coefficient

B. Primary-side ZVS

The MOSFETs on primary and secondary sides are soft-switched under different conditions. The nominal waveform of the current across the primary leakage inductor is re-illustrated in Fig. 3a. The phase shift d and duty cycle adjustment θ developed from [3] are applied. The primary switch S_2 is turned on at the time instance $[(n+0.5)T-\theta]$, and to achieve the ZVS, the current has to flow in the direction depicted in Fig. 3c, in order to discharge the parasitic capacitor C_{oss2} before S_2 is turned on, where switching period is denoted as T and n is the n-th switching instance. The required current direction accordingly demands the current to be larger than the commutating current I_{cm} that fully discharges the parasitic capacitor of the MOSFET that is softly turned on. Similarly, before primary switch S_1 is switched on, the current should be reversed and larger than I_{cm}. The amplitude of the commutating current is dependent on the switch voltage v_{ds}, parasitic capacitance C_{oss} and desired deadtime t_{dead}. For the operation in Fig. 3d, at the beginning of discharging/charging the parasitic capacitors, the primary leakage inductor current is divided into two branches, i.e. the switch to be turned on S_1 and the switch to be turned off S_2

$$i_{lk1}(t) = i_{oss1} + i_{oss2} = C_{oss2}\frac{dv_{oss2}}{dt} - C_{oss1}\frac{dv_{oss1}}{dt}. \quad (1)$$

It can be integrated over the deadtime t_{dead} during which the soft commutating is allowed to complete

$$\int_0^{t_{dead}} i_{lk2}(t)dt = \int_0^{V_\Sigma} C_{oss2}dv_{oss2} - \int_{V_\Sigma}^{0} C_{oss1}dv_{oss1} \quad (2)$$

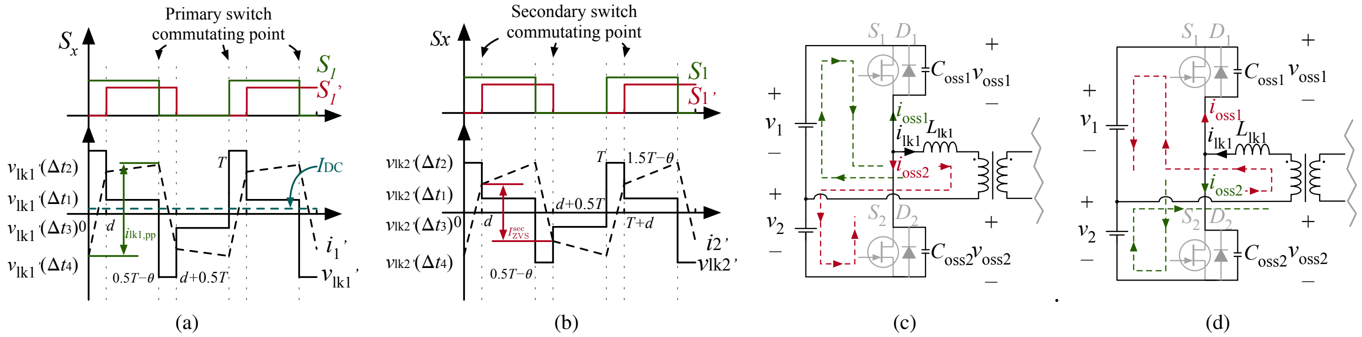

Fig. 3: (a) the primary leakage inductor current waveform (b) the primary-referred secondary leakage inductor current waveform (c) primary ECM at time instance $0.5T-\theta$, (d) primary ECM at time instance T

Assuming the leakage inductor current during the dead time is constant, it can further be simplified as

$$I_{\text{cm}} = \frac{V_{\Sigma}(C_{\text{oss1}} + C_{\text{oss2}})}{t_{\text{dead}}}. \tag{3}$$

Therefore, given the ripple component $i_{\text{lk1,pp}}$ and the direct current (DC) component I_{DC} of i_{lk1}, the condition for achieving ZVS on primary-side switches is

$$I_{\text{ZVS}}^{\text{pri}} = i_{\text{pp,lk1}} \geq I_{\text{DC}} + 2I_{\text{cm}} \tag{4}$$

where I_{DC} also regulates the net difference between two neighboring cells to realize different battery balancing modes [3]. In addition, $i_{\text{pp,lk1}}$ is obtained by calculating the increment of i_{lk1} during $[0, 0.5T-\theta]$ and given below:

$$i_{\text{lk1,pp}} = \frac{1}{f_{\text{s}}L_{\text{lk1}}(k+1)}\left[V_2 + V_{\text{o}}'d'k - \frac{V_2(V_2 + V_{\text{o}}'k)}{V_1+V_2}\right] \tag{5}$$

where V_1 and V_2 are the upper and lower bridge voltages, respectively, and switching frequency is f_{s}. Normalized phase shift between primary and secondary switches is denoted as d' and is obtained by $d/0.5T$. If the ZVS over the entire operating region is desired, the minimum current ripple of i_{lk1} needs to satisfy the condition in (4).

C. Secondary-side ZVS

Similarly, the secondary-side switches can be soft-switched if the $I_{\text{ZVS}}^{\text{sec}\prime}$ in Fig. 3b meet the condition like (4). The derivation of the commutating current requirement is identical to the primary side due to the symmetry of the topology. The minimum required amplitude for secondary switches can be simplified due to the absence of the DC bias current as shown below

$$I_{\text{ZVS}}^{\text{sec}\prime} \geq 2aI_{\text{cm}}. \tag{6}$$

The expression of $I_{\text{ZVS}}^{\text{sec}\prime}$ can be obtained by analyzing the waveform:

$$I_{\text{ZVS}}^{\text{sec}\prime} = \frac{T\left[k\left(V_1+V_2\right)d - kV_2 + V_{\text{o}}'\right]}{2L_{\text{lk2}}'a(k+1)}. \tag{7}$$

If the operating conditions, such as V_1, V_2 and V_{o}', are given, the combination of the switching period T and phase shift d that are regulated by the output power requirement can determine the soft-switching capability. The output power can be calculated using similar methods proposed in [3], [4], [15] and is shown here:

$$P_{\text{o}} = \frac{k}{k+1}\frac{1}{16af_{\text{s}}L_{\text{lk1}}}V_{\text{LV}}(V_1\alpha_{\text{lk2}}^{i_{\text{o}}} + V_2\beta_{\text{lk2}}^{i_{\text{o}}}) \tag{8}$$

where the coefficients $\alpha_{\text{lk2}}^{i_{\text{o}}}$ and $\beta_{\text{lk2}}^{i_{\text{o}}}$ are defined in Appendix.

III. Power Losses vs. Frequency Variation

In order to simplify the VFM and take conduction losses into account, the sources of the power losses from the circuit should be identified. The frequency dependency on each loss component needs to be analyzed so that the simplified control law can capture the most dominant effects without sacrificing the system efficiency.

A. Transformers

The losses of the transformers consist of conduction loss and core loss. Both of them are proved to be non-linearly frequency-dependent. However, if the net effect of both losses with the varying frequency can be identified, a simpler control law can be developed without the comprehensive modeling.

1) Conduction loss: The conduction loss is frequency dependent due to the skin and proximity effects developed on the conductor at high frequencies [16]. The total conduction losses due to the DC and AC resistances can be represented by

$$\begin{aligned} P_{\text{cu}}^{\text{trans}} =& R_{\text{DC}}^{\text{pri}}\sum_{k=0}^{+\infty}F_{\text{r}}^{\text{pri}}(f_{\text{k}})I_{\text{lk1,rms}}^2(f_{\text{k}}) \\ &+ R_{\text{DC}}^{\text{sec}}\sum_{k=0}^{+\infty}F_{\text{r}}^{\text{sec}}(f_{\text{k}})I_{\text{lk2,rms}}^2(f_{\text{k}}) \end{aligned} \tag{9}$$

where $F_{\text{r}}^{\text{pri}}(f_{\text{k}})$ is the primary-side AC/DC resistance ratio at the kth harmonic frequency f_{k}. Similarly, $F_{\text{r}}^{\text{sec}}(f_{\text{k}})$ is the secondary-side AC/DC resistance ratio at the kth harmonic frequency f_{k}. DC component is evaluated at f_0. The RMS currents at frequency f_{s} for primary and secondary sides are denoted as $I_{\text{lk1,rms}}(f_{\text{k}})$ and $I_{\text{lk2,rms}}(f_{\text{k}})$, which are calculated by the Fourier Series of the leakage inductor currents. The detailed Fourier Series of the leakage inductor currents is analyzed and given in [17]. The derivations in [17] show that the higher-order RMS component can be represented by the fundamental one.

$$I^2_{\text{lkx,rms}}(f_\text{k}) = \frac{I^2_{\text{lkx,rms}}(f_1)}{k^4},\ k \in \mathbb{Z}^+,\ x \in \{1,2\} \tag{10}$$

The total RMS currents are the geometrical summations of the RMS currents at each harmonic frequency, i.e.

$$I^2_{\text{lkx,rms}} = \underbrace{I_{\text{lkx,rms}}(f_0)^2}_{\text{DC component}} + I_{\text{lkx,rms}}(f_1)^2 + \underbrace{I_{\text{lkx,rms}}(f_2)^2 + \ldots}_{\text{negligible}} \tag{11}$$

The DC component in the equation above is frequency independent but balancing-mode dependent [3]. In addition, the DC component on the secondary side does not exist. As a result, the transformer copper loss can be simplified to

$$\begin{aligned} P^{\text{trans}}_{\text{cu}} =& R^{\text{pri}}_{\text{DC}} I^2_{\text{DC}} + R^{\text{pri}}_{\text{DC}} F^{\text{pri}}_{\text{r}}(f_\text{s}) I^2_{\text{lk1,rms}} \\ &+ R^{\text{sec}}_{\text{DC}} F^{\text{sec}}_{\text{r}}(f_\text{s}) I^2_{\text{lk2,rms}}. \end{aligned} \tag{12}$$

The RMS currents of the leakage inductors are inversely proportional to the switching frequency f_s given an operating condition [3], [4], [13]. The Fig. 4a shows the per-unit change of the products of $F^{\text{pri}}_{\text{r}} f_\text{s} I^2_{\text{lk1,rms}}$ and $F^{\text{sec}}_{\text{r}} f_\text{s} I^2_{\text{lk2,rms}}$ as the switching frequency increases for a planar printed circuit board (PCB) transformer [3]. It suggests that the overall conduction loss of the transformer significantly decreases as the switching frequency ascends.

2) Core loss: The core loss is a function of switching frequency and the peak flux density swing according to Steinmetz equation [18]. For a given transformer design, the flux density is then dependent on the operating frequency based on the Faraday's Law [16]. Therefore, the core loss at different frequencies of a cored transformer design with the size of EP38 and the core material of 3F46 from Ferroxcube [3] can be calculated and plotted in Fig. 4b. It shows that the core loss increases as the frequency rises up. The core loss however is relatively negligible compared with the conduction losses. This can be explained by the fact that the voltage which introduces the flux density swing is as low as a cell's voltage. As a result, the core loss for the transformers that are operating at low voltage, in general, can be approximated independent of the operating frequency. On the other hand, the coreless transformers inherently have no core losses. Therefore, varying frequency will not introduce extra core losses on the transformer.

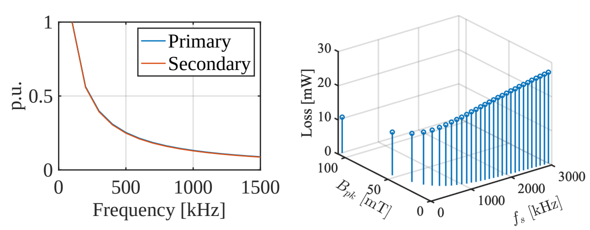

(a) (b)

Fig. 4: (a) The p.u. changes of products $F^{\text{pri}}_{\text{r}}(f_\text{s}) I^2_{\text{lk1,rms}}$ and $F^{\text{sec}}_{\text{r}}(f_\text{s}) I^2_{\text{lk1,rms}}$ as switching frequency increases for the cored transformer in [3]; (b) the core loss varying with frequency

B. Power switches

The losses of the power switches consist of the conduction losses due to the resistance when it is conducting, and the switching loss during the switching transient.

1) Conduction loss: Similar with the analysis conducted previously, the conduction loss of the power switches is calculated by

$$P^{\text{MOS}}_{\text{cu}} = R_{\text{ds,on}} \left(n^{\text{pri}}_{\text{HB}} I^2_{\text{lk1,rms}} + n^{\text{sec}}_{\text{HB}} I^2_{\text{lk2,rms}} \right) \tag{13}$$

where, $R_{\text{ds,on}}$ is the turn-on resistance of the power MOSFET. Assuming the switches are identical on both primary and secondary sides, the resistances are approximated the same. Otherwise, each MOSFET's on-resistance should be substituted. The numbers of half-bridge on primary and secondary side are denoted as $n^{\text{pri}}_{\text{HB}}$ and $n^{\text{sec}}_{\text{HB}}$, respectively. For example, for the DAHB configuration, $n^{\text{pri}}_{\text{HB}} = 1$ and $n^{\text{sec}}_{\text{HB}} = 1$. As the frequency increases, the leakage inductor RMS current decreases according to the previous analysis [3], [4], [13], leading to less MOSFET conduction loss.

2) Switching loss: The switching loss consists of turn-on loss of MOSFET $P^{\text{MOS}}_{\text{on}}$, turn-off loss of MOSFET $P^{\text{MOS}}_{\text{off}}$, diode reverse recovery loss $P^{\text{Diode}}_{\text{rr}}$, dead-time loss $P^{\text{Diode}}_{\text{dt}}$ and driver loss P_{dr}, i.e.

$$P^{\text{MOS}}_{\text{swi}} = P^{\text{MOS}}_{\text{on}} + P^{\text{MOS}}_{\text{off}} + P^{\text{Diode}}_{\text{rr}} + P^{\text{Diode}}_{\text{dt}} + P_{\text{dr}} \tag{14}$$

Turn-on and turn-off losses can be calculated by [18], [19]

$$P^{\text{MOS}}_{\text{on}} = \begin{cases} (f_\text{s} I_{\text{Don}}) \left(U_{\text{DD}} \frac{t_{\text{ri}}+t_{\text{fu}}}{2} \right) & \text{, hard switching} \\ 0 & \text{, full soft switching} \end{cases} \tag{15}$$

$$P^{\text{MOS}}_{\text{off}} = (f_\text{s} I_{\text{Doff}}) \left(U_{\text{DD}} \frac{t_{\text{ru}}+t_{\text{fi}}}{2} \right), \tag{16}$$

where the rising times of the switch voltage and current are denoted as t_{ru} and t_{ri}. Similarly, the falling times of the switch voltage and current are t_{fu} and t_{fi}. Drain currents at turn-on and turn-off instances are defined as I_{Don} and I_{Doff}, respectively. Other than full soft switching and hard switching, partial soft switching, when (3) is not entirely satisfied, results in losses higher than full soft switching but lower than hard switching. This partial soft switching is analyzed in [11]. However, full soft switching is guaranteed by MPPA and will be explained in Section V, so it is excluded in the analysis.

The rising and falling time characteristics are mainly dependent on the switching voltage and the intrinsic properties of the switch device, such as gate threshold voltage and gate charges [18]. As long as the switching voltage maintains the same level, the rising and falling characteristics are expected to be roughly constant with the varying frequency, which will be explained by the measurement of the turn-on/off energy shown in Section VI-C.

Gate driver and snubber designs also play significant roles in the switching losses. Therefore, a well-designed gate driver and snubber can reduce the switching losses drastically. The dependency on the gate driver and snubber designs is, however, excluded in this study as it is assumed that the circuit under evaluation is identical for all the control strategies.

The previous analysis has shown that the currents on primary and secondary sides are inversely proportional to the operating frequency as shown in (5) and (7). That is,

$$I_{\text{Don}}^{\text{pri}} = \frac{I_{\text{ZVS}}^{\text{pri}} - I_{\text{DC}}}{2} \propto \frac{1}{f_{\text{s}}}, \tag{17}$$

$$I_{\text{Don}}^{\text{sec}} = \frac{I_{\text{ZVS}}^{\text{sec}}}{2} \propto \frac{1}{f_{\text{s}}}. \tag{18}$$

Note that turn-on current for one-side switch approximately equals to the turn-off current for the complimentary switch. Substituting the equations in (15) and (16) yields the MOSFETs turn-on and turn-off losses that are independent on the switching frequency. They can be approximated as constant if the rising and falling timing characteristics stay stable across the operating frequencies. Therefore, the only two losses that increase with increasing switching frequency are the reverse recovery power loss $P_{\text{rr}}^{\text{Diode}}$ and gate driver loss P_{dr}. In particular, eGaN semiconductors do not have body diodes therefore there are no reverse recovery losses. The reverse conduction capability is achieved by a different mechanism in eGaN devices [20]. On the other hand, the gate driver loss is relatively low compared with other losses. For example, the estimated gate driver loss using a commercially available GaN/SiC gate driver IC LM5113 is around 0.092 W for 100 kHz operation and 0.92 W for 1 MHz operation with a 1000 pF capacitive load and a 10 nC gate charge [21]. The reverse recovery power loss $P_{\text{rr}}^{\text{Diode}}$ and gate driver loss P_{dr} are considered negligible [22]. Dead-time loss is determined by the forward voltage of the body-diode V_f, conducting current (approximately current at switching instance [23]), as well as the dead time t_{dt}:

$$P_{\text{dt}} = V_f I_D f_s t_{\text{dt}}. \tag{19}$$

Based on (17) and (18), the dead-time loss is frequency-independent and negligible compared with conduction losses. Therefore, the overall trend of the total power loss as switching frequency increases is diminishing. The change of each loss component with respect to the increasing operating frequency is summarized in Table II.

TABLE II: The effect of increasing frequency on categorized losses

Loss	Changing direction
Transformer Cu	$\downarrow$
Transformer Core	$\rightarrow$
MOSFET Cu	$\downarrow$
MOSFET switching	$\rightarrow$

IV. The power per ampere criteria

Based on the previous analysis, the total loss of the system can be approximated to decrease as the frequency increases. In particular, the leakage inductor RMS currents determine the conduction loss that is a major part of the total loss [22]. Therefore, given a certain output power level, the operating condition resulting in the minimum RMS current theoretically will lead to the lowest total loss in the system. A simple mathematical expression can summarize this statement. That is,

$$\begin{aligned} MPPA(\phi) &= \max(PPA(\phi)) \\ &= \max\left(\frac{P_{\text{o}}(\phi, f_{\text{s}})}{\sqrt{I_{\text{lk1,rms}}^2(\phi, f_{\text{s}}) + I_{\text{lk2,rms}}^2(\phi, f_{\text{s}})}}\right) \end{aligned} \tag{20}$$

where $\phi = [d, V_1, V_2, V_{\text{o}}]$. The transformer RMS currents on primary- and secondary-side are denoted as $I_{\text{lk1,rms}}$ and $I_{\text{lk2,rms}}$, respectively. $PPA(\phi)$ is the equation describing the ratio between output power and total RMS current and named as ***power per ampere*** in this study. Note that $PPA(\phi)$ is only the function of ϕ as the frequency dependence in P_o and $I_{\text{lkx,rms}}$ is canceled out during the operation. It can be seen that PPA increases with higher output power and lower total RMS current, which is consistent with minimizing the total RMS current to improve the system efficiency. Since (20) attempts to maximize the output power over the total RMS current, this method is named as ***maximum power per ampere***. For a given operating condition, e.g. cell voltages and switching frequency, the (20) tries to locate the phase shift d that achieves the largest PPA ratio, at which the system should operate with the minimum conduction loss at a given power level.

A. Transformer RMS currents

The transformer RMS currents determine the conduction losses on the transformer as well as the MOSFETs. Also, in order to locate the optimal solution for (20), the models for the transformer RMS currents are needed. They can be obtained by piece-wisely integrating the squared current functions and shown in (21) and (22).

B. Switching frequency independence

After substituting the output power and RMS current equations from (8) and (21) and (22), the detailed expression of the PPA function can be obtained. Then the MPPA point is located by a non-linear optimization algorithm. Finding the maximum of a positive function is equivalent to find the maximum of the squared of the function. Therefore, in order to simplify the expression of PPA, the squared PPA is computed instead.

$$PPA^2(\phi) = V_{\text{o}}^2 \underbrace{\frac{k^2\left[\alpha_3^{\text{PPA}} d^2 + \alpha_2^{\text{PPA}} d + \alpha_1^{\text{PPA}}\right]^2}{\beta_4^{\text{PPA}} d^3 + \beta_3^{\text{PPA}} d^2 + \beta_2^{\text{PPA}} d + \beta_1^{\text{PPA}}}}_{\frac{I_o^2(\phi, f_{\text{s}})}{I_{\text{lk1,rms}}^2(\phi, f_{\text{s}}) + I_{\text{lk2,rms}}^2(\phi, f_{\text{s}})}} \tag{23}$$

It should be noted that the (23) is independent on the operating frequency. Therefore, the MPPA points will not vary with the changing operating frequency. This is a critical property of the proposed MPPA so that the frequency is not coupled with the phase shift as the conventional VFM, which simplifies the control logic.

C. Cell voltage dependence

Instead, the MPPA points only rely on the operating conditions, such as the cell voltages and phase shift. The cell voltages can be approximated as constant during one switching period and are measurable parameters in (23). It is thus arranged as an expression of phase shift only. As a result, the MPPA point at given cell voltages are only determined by the phase shift d.

V. THE SOLUTION FOR MPPA OPTIMIZATION

Provided the operating conditions, the MPPA points can be solved based on (23). The equation is significantly non-linear. However, the approximations to (23) can be applied in order to implement the online calculation of MPPA without drastically sacrificing the accuracy. The system specifications and parameters are shown in Tables I and III.

TABLE III: System parameters

Parameter	Value
Effective turns ratio a	3.74
Magnetization inductance L_m	141.5 nH
Leakage inductance L_{lk1}	24.9 nH
coupling coefficient k	0.85
Input and output capacitors C_1 - C_4	6.3 uF
PI controller	$K_p = 100$ and $K_i = 1e7$
Input voltages V_1 and V_2	3.3 - 4.2 V
Switching frequency f_s	100 - 1000 kHz

A. Full-order system

The non-linear optimization algorithm, such as sequential quadratic programming, can be applied to locate the phase shifts where the MPPA is satisfied using (23) to generate the pre-calculated phase shift LUT for online implementation.

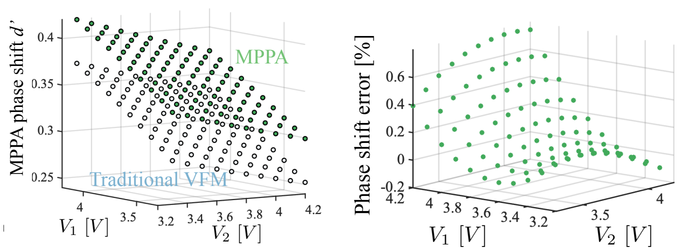

(a) (b)

Fig. 5: (a) Operating phase shifts generated from the MPPA and critical soft switching with different cell voltages, (b) MPPA phase shift error between 2nd-order model and full-order expanded at d = 0.35 when $V_{\text{LV}} = 12$ V

As an example, a MPPA phase shift plot is shown in Fig. 5a based on a transformer with the circuit parameters specified in Table III. However, other transformer designs can be substituted to obtain the MPPA phase shifts at different voltage combinations. It can be seen from the plot that the MPPA phase shift varies with the cell voltages, and LV/output capacitor voltage. The MPPA phase shift is minimum when cell 1 is at the maximum voltage while cell 2 is at the lowest one. This can be explained by the shifted peak power if the cells are out of balance [3], [24]. The peak power is achieved at smaller phase shift when $V_1 > V_2$ and vice versa. So this MPPA map can be extracted as a LUT to find the desired phase shift when the cell voltages are measured. In addition, the phase shifts that satisfy the minimum requirement of ZVS in (6) (critical soft switching) are illustrated in light black in Fig. 5a. As it can be seen from the plot, the operating points MPPA suggests are always higher than the ones generated from critical soft switching. That is, MPPA guarantees ZVS operation, leading to minimized turn-on losses.

B. Reduced-order systems for computation-restrained environments

The reduced-order PPA expression can be obtained by applying Taylor Series Expansion at a quiescent operating condition, whose maximum can be computed in the real-time controllers.

1) 1st-order Taylor Series Expansion: The first-order Taylor approximation is applied on (23) at the nominal condition where $\phi_{\text{q}} = [0.25, 3.6, 3.6, 6.5]$. Since it is a first-order approximation, the linear relationship constantly generates the MPPA phase shift at its maximum 0.5. The errors are not negligible especially at extreme conditions. Therefore, it is not practical to implement due to its high error.

2) 2nd-order Taylor Series Expansion: In order to overcome the drawback of the first-order approximation, the second-order Taylor Series Expansion can be applied on the full-order model. The second-order model can be improved by adjusting the quiescent point where it is expanded as the MPPA phase shift points locate around 0.35 based on the full-order model in Fig. 5a. The error between the updated second-order model and the full-order model is given in Fig. 5b, which is more accurate than the previous model. The maximum is located where the derivative with respective to d equals 0, i.e.

$$d_{\text{MPPA}}^{\text{2nd}} = 0.0931V_2 - 0.0458V_1 - 0.0278V_{\text{o}} + 0.35. \tag{24}$$

This form can be directly implemented in the real-time controller without putting much computational burden on it.

3) Higher-order Taylor Series Expansion: Higher-order models are expected to have higher accuracy. However, the higher complexity it introduces makes implementing it on the embedded systems infeasible. Therefore, it is excluded in

$$I_{\text{lk1,rms}} = \frac{T}{4\sqrt{3}L_{\text{lk1}}(V_1+V_2)(k+1)}\sqrt{k^2V_{\text{o}}'^2(V_1+V_2)^2 + 4a^2V_1^2V_2^2 - 4akV_{\text{o}}'\Gamma} \tag{21}$$

$$I_{\text{lk2,rms}} = \frac{T}{4\sqrt{3}L_{\text{lk2}}a(V_1+V_2)(k+1)}\sqrt{V_{\text{o}}'^2(V_1+V_2)^2 + 4a^2k^2V_1^2V_2^2 - 4akV_{\text{o}}'\Gamma} \tag{22}$$

this study. The flowcharts for implementing the full-order and reduced-order MPPA are illustrated in Fig. 6.

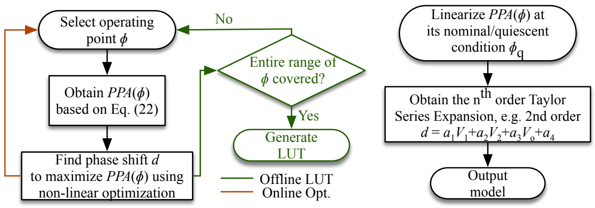

Fig. 6: The flowcharts for (a) full-order and (b) reduced-order MPPA optimizations

VI. MPPA-BASED VARIABLE FREQUENCY MODULATION

A. Proposed methodology

It has been shown that the MPPA is only dependent on the cell voltages and phase shift, regardless of the operating frequency. The phase shift generated from MPPA guarantees the maximum RMS utilization and thus, the minimized conduction loss are obtained at the MPPA operating point. However, if the frequency is introduced as a variable, the conduction loss due to the RMS currents can be also reduced with a higher operating frequency shown in (21) and (22) as they are inversely proportional to the operating frequency f_s. Even though phase shift also determines output power, the combination of increasing operating frequency and phase shift not only maintains output power but also decreases RMS current, as mathematically predicted in power equation (8). Figure 7 shows RMS currents at different operating frequencies for a constant 10W output, covering the input and output voltage ranges specified in Table III. It can be seen that higher switching frequency results in significantly less RMS current while keeping output power constant.

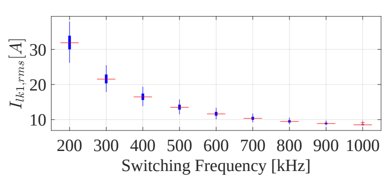

Fig. 7: The RMS current distributions at different switching frequencies for a constant 10-W output

If the switching loss stays relatively constant as analyzed in the previous section, the total loss of the system largely relies on the conduction loss. Therefore, the VFM algorithm can be simplified to directly adjusting the frequency to satisfy the requirement of the output power given an operating phase shift defined by MPPA. The control architecture for the conventional critical VFM and the direct MPPA-based VFM are plotted Fig. 9. The operating frequency is controlled based on the resulting output power P_o. When the output power is lower than the reference, the frequency slightly drops to accommodate the error, and vice versa. This mechanism is achieved by a closed-loop PI controller in this study, which is designed by investigating the small-signal model and applying Bode-Plot analysis for stability analysis, refer to Appendix for details. The open-loop Bode plots combined with PI controller (parameters shown in Table I) are shown in Fig. 8. Multiple operating points are swept to evaluate the overall system stability. It can be seen that all operating points are stable with crossover frequency at least an order of magnitude of 2 smaller than sampling frequency 200 kHz.

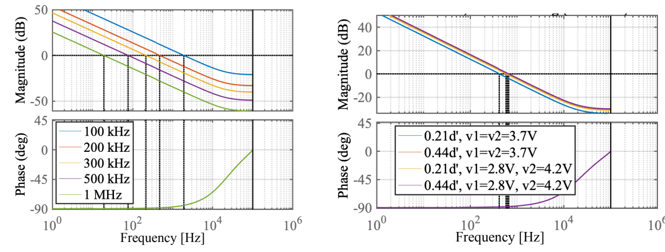

Fig. 8: The combined system open-loop Bode plots with different quiescent points: (a) varying switching frequency and (b) varying phase shift and input voltages

Note that the operating frequency should be bounded by upper and lower limits beyond which the semiconductor devices might be damaged. On the other hand, the conventional critical VFM is shown in Fig. 9b. It can be seen that the 4D-LUT is applied to obtain the operating variables d and f_s and it is operated in an open-loop fashion. Therefore, any disturbance from the modeling would affect the final outcome. Using MPPA, the switching frequency can be back-calculated by (8) given the operating conditions, and transformer parameters.

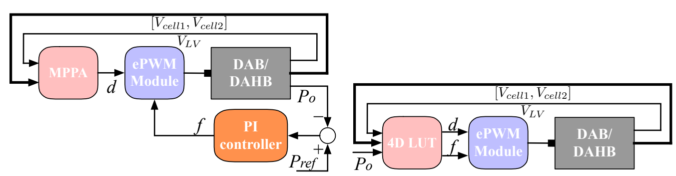

Fig. 9: The control architecture with (a) direct MPPA-based VFM (b) conventional critical VFM

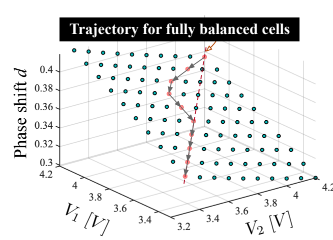

Fig. 10: The example trajectory of MPPA phase shift as the cells discharge from full

B. Operation example for a battery balancing application

An example of the trajectory that MPPA phase shift would follow when the cells discharge from fully charged is given in

Fig. 10. It is assumed that the two cells in one link are both at full charge, i.e. 4.2 V. Due to the nonidentical capacities or internal impedances, the voltages of the cells start to deviate from the trajectory of the cells with exactly identical voltages as they discharge. As a result, the MPPA phase shift is adjusted to the optimal points based on the cell voltages for a period of time. Once the cells voltages are corrected by the balancing mechanism, the diagonal MPPA trajectory is resumed until the batteries are below the minimum voltage where the rated power is provided or the voltages are unbalanced again. Note that the switching frequency is also varying to guarantee the output power capability.

C. Comparison with traditional VFM

The critical soft-switching commonly solves for the phase shift and switching frequency that allow the soft switching with a boundary condition where the current at the switching instance satisfies the ZVS requirement. Fig. 5a shows the phase shifts generated from traditional VFM with a 0.5 A ZVS current requirement are smaller than the ones produced by MPPA. The ZVS requirement on the secondary leakage inductor current is obtained based on the parasitic parameters of the GaN MOSFETs used in the testbench.

Given the parasitic capacitance is 1450 pF for EPC 2021 [25], the required ZVS current for a dead time of 70 ns is 0.5 A based on (3), where 70 ns is 3.5% of the period of 500 kHz switching. It is noted that the required ZVS current may vary based on the different parasitic values, but for a low-voltage and fast MOSFETs the ZVS current is expected to be similar.

The calculated phase shifts based on the traditional VFM are worst-condition values which are obtained at maximum operating frequency, as higher phase shift is required to achieve soft switching at higher frequency, which can be explained by (7). Therefore, the phase shifts that are optimized by MPPA criteria equivalently increase the soft switching capability, which in turn makes the statement rigorous that switching loss is relatively constant over a wide frequency range as explained in the previous section.

The PPA at the point that is generated by the critical soft-switching is not often maximized, leading to higher conduction losses. It can be also seen from Fig. 5a that applying MPPA not only reduces the conduction losses at the given operating frequency but also ensures the ZVS.

An example of per-unit (p.u.) loss distributions between MPPA-VFM and critical VFM is plotted in Fig. 11a. All the losses are normalized with respect to the primary-side MOSFET conduction loss at 20% output power. Only turn-off switching loss is considered in this analysis and is obtained by the double pulse test at the different switching currents, as shown in Fig. 11b. It shows that the turn-on/off energy is an approximately linear function of the amplitude of switched current, which proves the rising and falling time characteristics for switching period barely changes shown in (15). It can be seen from Fig. 11a, as the switching current reduces the energy is also reduced, which is consistent with the derivation in Section III-B2. It is assumed that the primary- and secondary-side MOSFETs are identical such that the $R_{\mathrm{ds,on}}$ is the same for

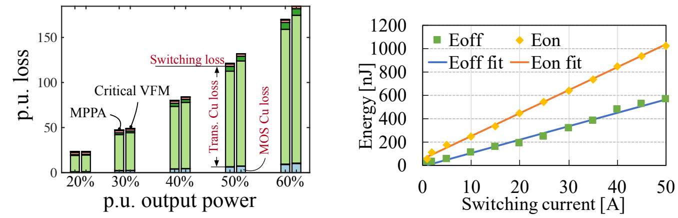

(a) (b)

Fig. 11: (a) The example p.u. loss distribution between MPPA-VFM and critical VFM at different power levels; (b) The extracted switching energy from double pulse test compared with linearly fitted models

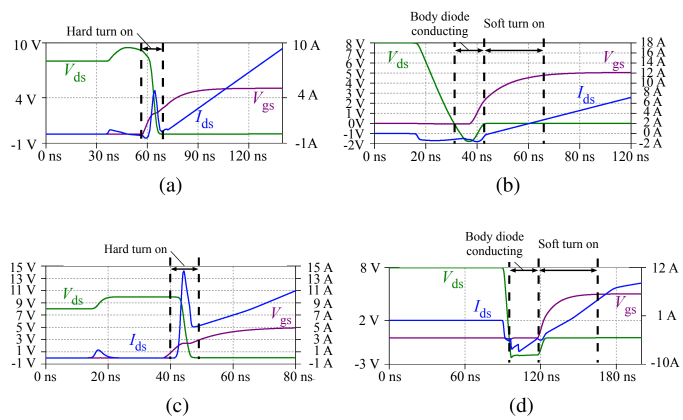

Fig. 12: Primary switching transitions: (a) high-side hard turn-on for comparison ($I_{\mathrm{lk1}}(0) > 0$); (b) high-side soft turn-on ((4) is satisfied); (c) low-side hard turn-on for comparison ($I_{\mathrm{lk1}}(0.5T - \theta) < 0$); (d) low-side soft turn-on ((4) is satisfied)

simplicity. It can be seen from the plot, the most dominant loss is the conduction losses from MOSFET and transformer. At high power load, the advantage of maximizing PPA appears, leading to lower p.u. loss compared with critical VFM.

VII. Experimental validation

Experiments are conducted on a self-developed DAHB testbench with coreless transformer, as shown in Fig. 13a. The SiC789 integrated half-bridge modules are used with built-in gate drivers. The coreless transformer measurements are given in Table III .

A. Transformer current vs. frequency

To experimentally prove that increasing frequency not only decreases RMS current but also achieves ZVS, the transformer current waveforms are captured on Fig. 13 given the same output power demand. The test is performed with input voltages of 4 V and LV voltage of 12 V at a constant 13-W output. The figures show the primary transformer ripple current I_{lk1} approximately reduces by 50% with frequency doubled from 200 kHz to 400 kHz, which can be mathematically explained by (5). It keeps decreasing as the frequency rises. On the other hand, at low load condition, ZVS condition is more

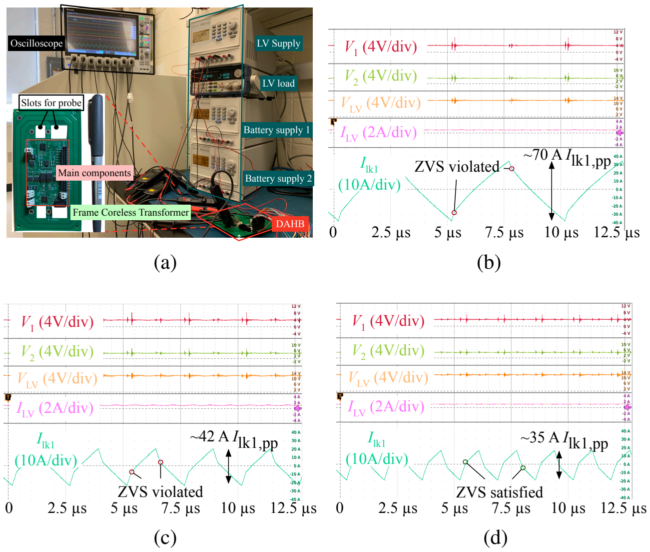

Fig. 13: (a) DAHB testbench with the coreless transformer; scope captures at 13-W constant output power at switching frequency of (b) 200 kHz (c) 400 kHz (d) 600 kHz

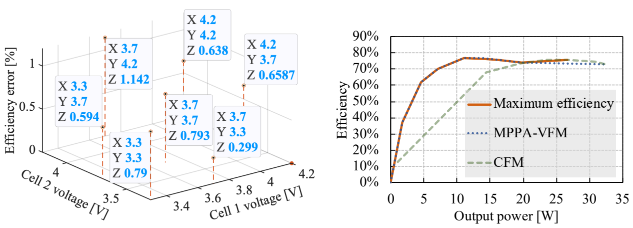

Fig. 14: (a) Difference between ground-true maximum efficiency and MPPA efficiency; (b) Comparison of ground-true maximum efficiency, MPPA-VFM and CFM

difficult to satisfy as shown in Figs. 13b and 13c whereas the switches are soft switched at 600 kHz in Fig. 13d, leading to higher efficiency. The actual ZVS transition is inaccessible due to the compact and integrated package of the SiC789 half-bridge module. The SPICE model is used to evaluate the ZVS transition. Fig. 12 shows the hard and soft switching waveforms on primary switches where (4) is violated and satisfied, respectively.

B. MPPA vs. actual maximum efficiency

To verify applying MPPA can operate the system at its pseudo optimal efficiency, the maximum system efficiencies at different input voltages are experimentally obtained. With each voltage combination, the efficiency recorded operating at MPPA phase shift is compared with the actual maximum efficiency by sweeping the entire phase shift range, as shown in Fig. 14a. It shows that the MPPA method provides a 0.61% of average efficiency offset compared with the ground-true maximum efficiency. Therefore, this method can provide the approximate maximum efficiency at a given frequency. A comparison among the maximum efficiencies from ground-true, MPPA-VFM and CFM is illustrated in Fig. 14b. The

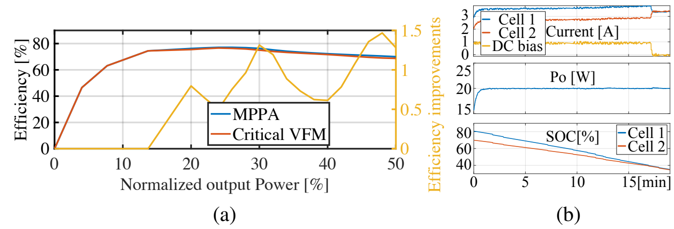

Fig. 15: (a) Comparison between critical VFM and MPPA-VFM at low load conditions; (b) Balancing evaluation result

CFM is operating at 300kHz constantly whereas the MPPA-VFM dynamically adjusts the frequency based on the required output power.

From Fig. 14b, the results show that the CFM is inefficient at light load condition as power is mainly dissipated on the switching and conduction. Instead, the MPPA-VFM increases the frequency to decrease the RMS current and soft switch, leading to a higher efficiency when the load is low. When the load increases, the efficiencies of CFM and VFM merge since the switching frequency decreases to its minimum 300 kHz.

C. Light-load operation compared with critical soft-switching

The critical VFM is also experimentally compared with MPPA-based VFM at low load conditions with the normalized output power between 20% - 50%, as shown in Fig. 15a. It shows that MPPA-based VFM improves the efficiency up to 1.5% from 10% to 50% of the peak load, thanks to the reduced effective-power-to-RMS ratio. The balancing evaluation on two 10-% unbalanced 3-Ah cells is also illustrated in Fig. 15b. The imbalance can be corrected within 20 mins.

VIII. Conclusion and Cost Discussion

This study proposes a simplified variable frequency modulation that maximizes the effective total RMS current at a given switching frequency while maintaining soft-switching. The output power can be controlled by regulating the frequency and the phase shift is set based on MPPA points. The approximated MPPA expressions based on Taylor Series Expansion are given to achieve online estimation. The MPPA-VFM shows similarly high efficiency compared with ground-true maximum efficiency. At least 1% improvement is gained from adopting MPPA-VFM while operating the system in a closed-loop fashion and with reasonable computational power.

Even though higher switching frequency can lead to higher cost on switching devices, it should be noted that the output power is also dependent on leakage inductance. Therefore, an optimally designed transformer can compensate and even lower the cost increased by switching devices. On the other hand, since a lower switching frequency leads to higher output power for a given transformer design, scaling up the power level shall not increase the overall cost.

Acknowledgment

The authors would like to acknowledge Bernard W. Steyaert for the support on the system analysis.

APPENDIX

The discrete-time state-space model of the system can be represented as follows:

$$\mathbf{x}[k+1] = f(\mathbf{x}[k], \mathbf{u}[k]),\ y[k] = g(\mathbf{x}[k], \mathbf{u}[k]) \tag{25}$$

$$\mathbf{x} = \begin{bmatrix} I_{\mathrm{lk1,t_0}} & I_{\mathrm{lk2,t_0}} \end{bmatrix}^T,\ \mathbf{u} = \begin{bmatrix} f_s & d' & \theta \end{bmatrix}^T,\ y = P_o \tag{26}$$

where $I_{\mathrm{lk1,t_0}}$ and $I_{\mathrm{lk2,t_0}}$ are the initial currents of primary-side and secondary-side leakage inductor during each switching period. The functions f and g are derived based on average modeling [26]. The non-linear system is linearized at a quiescent point $Q = [f_s, d', V_1, V_2]$ by first-order Taylor Expansion while omitting higher-order residue and constant bias.

$$\mathbf{x}[k{+}1] = \underbrace{\frac{\partial f}{\partial \mathbf{x}}|_Q}_{\mathbf{A}} \mathbf{x}[k] + \underbrace{\frac{\partial f}{\partial \mathbf{x}}|_Q}_{\mathbf{B}} \mathbf{u}[k],\ \mathbf{y}[k] = \underbrace{\frac{\partial g}{\partial \mathbf{x}}|_Q}_{\mathbf{C}} \mathbf{x}[k] + \underbrace{\frac{\partial g}{\partial \mathbf{x}}|_Q}_{\mathbf{D}} \mathbf{u}[k] \tag{27}$$

$$\left.\begin{array}{l} \mathbf{A} = \begin{bmatrix} 1 & 0 \\ 0 & 1 \end{bmatrix}, \mathbf{B} = \begin{bmatrix} 3.79e\text{-}4 & 0 & -1.51e8 \\ 3.22e\text{-}4 & 0 & -1.29e8 \end{bmatrix} \\ \mathbf{C} = \mathbf{0},\ \mathbf{D} = \begin{bmatrix} 4.2e\text{-}4 & -193.4 & -3.86e7 \end{bmatrix} \end{array}\right\} @\, Q^T = \begin{bmatrix} 200e3 \\ 0.22 \\ 2.8 \\ 4.2 \end{bmatrix} \tag{28}$$

The transfer function then can be calculated by $G(z) = \mathbf{C}(z\mathbf{I} - \mathbf{A})^{-1}\mathbf{B} + \mathbf{D}$. The coefficients in this study are defined below:

$$\alpha_3^{\mathrm{PPA}} = (V_1 + V_2)^2, \alpha_2^{\mathrm{PPA}} = -2V_2^2 - 2V_1V_2, \alpha_1^{\mathrm{PPA}} = V_2^2 - V_1V_2$$

$$\beta_4^{\mathrm{PPA}} = \frac{-5V_\mathrm{o}k}{196a}\left(V_1^3 + 3V_1^2V_2 + 3V_1V_2^2 + V_2^3\right)$$

$$\beta_3^{\mathrm{PPA}} = \frac{15V_\mathrm{o}k}{196a}\left(V_1^2V_2 + 2V_1V_2^2 + V_2^3\right)$$

$$\beta_2^{\mathrm{PPA}} = \frac{15V_\mathrm{o}k}{196a}\left(V_1^2V_2 - V_2^3\right)$$

$$\beta_1^{\mathrm{PPA}} = \frac{V_\mathrm{o}k}{196a^2}\beta + \frac{V_1^2V_2^2a^2 + V_\mathrm{o}^2(V_1+V_2)^2}{196a^2}$$

$$\beta = \left(V_\mathrm{o}kV_1^2 - 15aV_1V_2^2 + 2V_\mathrm{o}kV_1V_2 + 5aV_2^3 + V_\mathrm{o}kV_2^2\right)$$

$$\alpha_{\mathrm{lk2}}^{i_\mathrm{o}} = -1 + 4d' + 2\theta' - 2d'^2 - \theta'^2 - 4d'\theta'$$

$$\beta_{\mathrm{lk2}}^{i_\mathrm{o}} = 1 + 2\theta' - 2d'^2 - \theta'^2 - 4d'\theta'$$

REFERENCES

[1] M. Preindl, C. Danielson, and F. Borrelli, "Performance evaluation of battery balancing hardware," in *European Control Conference (ECC)*, pp. 4065–4070, 2013.

[2] M. Evzelman, M. M. Ur Rehman, K. Hathaway, R. Zane, D. Costinett, and D. Maksimovic, "Active Balancing System for Electric Vehicles With Incorporated Low-Voltage Bus," in *IEEE Applied Power Electronics Conference and Exposition*, DOI 10.1109/TPEL.2015.2513432, pp. 3230–3236, 2014.

[3] W. Wang and M. Preindl, "Dual Cell Links for Battery-Balancing Auxiliary Power Modules: A Cost-Effective Increase of Accessible Pack Capacity," *IEEE Transactions on Industry Applications*, vol. 56, DOI 10.1109/TIA.2019.2959728, no. 2, pp. 1752–1765, 2020.

[4] F. Z. Peng, H. Li, G. J. Su, and J. S. Lawler, "A new ZVS bidirectional DC-DC converter for fuel cell and battery application," *IEEE Transactions on Power Electronics*, vol. 19, DOI 10.1109/TPEL.2003.820550, no. 1, pp. 54–65, 2004.

[5] H. Li, F. Z. Peng, and J. S. Lawler, "A natural ZVS medium-power bidirectional DC-DC converter with minimum number of devices," *IEEE Transactions on Industry Applications*, vol. 39, DOI 10.1109/TIA.2003.808965, no. 2, pp. 525–535, 2003.

[6] S. S. Shah and S. Bhattacharya, "A simple unified model for generic operation of dual active bridge converter," *IEEE Transactions on Industrial Electronics*, vol. 66, DOI 10.1109/TIE.2018.2850012, no. 5, pp. 3486–3495, 2019.

[7] O. M. Hebala, A. A. Aboushady, K. H. Ahmed, and I. Abdelsalam, "Generic Closed-Loop Controller for Power Regulation in Dual Active Bridge DC-DC Converter With Current Stress Minimization," *IEEE Transactions on Industrial Electronics*, vol. 66, DOI 10.1109/TIE.2018.2860535, no. 6, pp. 4468–4478, 2019.

[8] X. Liu, Z. Q. Zhu, D. A. Stone, M. P. Foster, W. Q. Chu, I. Urquhart, and J. Greenough, "Novel Dual-Phase-Shift Control With Bidirectional Inner Phase Shifts for a Dual-Active-Bridge Converter Having Low Surge Current and Stable Power Control," *IEEE Transactions on Power Electronics*, vol. 32, DOI 10.1109/TPEL.2016.2593939, no. 5, pp. 4095–4106, 2017.

[9] X. F. He, Z. Zhang, Y. Y. Cai, and Y. F. Liu, "A variable switching frequency hybrid control for ZVS dual active bridge converters to achieve high efficiency in wide load range," *Conference Proceedings - IEEE Applied Power Electronics Conference and Exposition - APEC*, DOI 10.1109/APEC.2014.6803443, pp. 1095–1099, 2014.

[10] J. Hiltunen and V. Vesa, "Variable-Frequency Phase Shift Modulation of a Dual Active Bridge Converter," *IEEE Transactions on Power Electronics*, vol. 30, no. 12, pp. 7138–7148, 2015.

[11] B. Agrawal, L. Zhou, A. Emadi, and M. Preindl, "Variable-Frequency Critical Soft-Switching of Wide-Bandgap Devices for Efficient High-Frequency Nonisolated DC-DC Converters," *IEEE Transactions on Vehicular Technology*, vol. 69, DOI 10.1109/TVT.2020.2987028, no. 6, pp. 6094–6106, Jun. 2020.

[12] K. Kim and H. Cha, "Split-Capacitor Dual-Active-Bridge Converter," *IEEE Transactions on Industrial Electronics*, vol. 0046, DOI 10.1109/TIE.2020.2969118, no. c, pp. 1–1, 2020.

[13] R. T. Naayagi, A. J. Forsyth, and R. Shuttleworth, "High-power bidirectional DC-DC converter for aerospace applications," *IEEE Transactions on Power Electronics*, vol. 27, DOI 10.1109/TPEL.2012.2184771, no. 11, pp. 4366–4379, 2012.

[14] D. Gilabert-Palmer, E. Sanchis-Kilders, V. Esteve, A. Ferreres, J. B. Ejea, E. Maset, J. Jordn, and E. Dede, "Measuring Coupling Coefficient of Windings with Dissimilar Turns' Number or Tight Coupling Using Resonance," *IEEE Transactions on Power Electronics*, vol. 33, DOI 10.1109/TPEL.2018.2794621, no. 11, pp. 9790–9802, 2018.

[15] L. Xue, D. Boroyevich, and P. Mattavelli, "Switching condition and loss modeling of GaN-based dual active bridge converter for PHEV charger," *Conference Proceedings - IEEE Applied Power Electronics Conference and Exposition - APEC*, vol. 2016-May, DOI 10.1109/APEC.2016.7468038, pp. 1315–1322, 2016.

[16] W. G. Hurley and W. H. Wölfle, *Transformers and Inductors for Power Electronics*. Chichester, UK: John Wiley & Sons, Ltd, Mar. 2013.

[17] J. Everts, G. E. Sfakianakis, and E. A. Lomonova, "Using fourier series to derive optimal soft-switching modulation schemes for dual active bridge converters," in *2015 IEEE Energy Conversion Congress and Exposition, ECCE 2015*, DOI 10.1109/ECCE.2015.7310317, pp. 4648–4655.

[18] R. Hou and A. Emadi, "Evaluation of Integrated Active Filter Auxiliary Power Modules in Electrified Vehicle Applications," Thesis, McMaster University, 2015.

[19] D. Graovac, M. Pürschel, and K. Andreas, "MOSFET Power Losses Calculation Using the Data- Sheet Parameters," *Infineon Technologies AG*, no. July, pp. 1–23, 2006.

[20] J. Chen, Q. Luo, J. Huang, Q. He, and X. Du, "A Complete Switching Analytical Model of Low-Voltage eGaN HEMTs and Its Application in Loss Analysis," *IEEE Transactions on Industrial Electronics*, vol. 67, DOI 10.1109/TIE.2019.2891466, no. 2, pp. 1615–1625, 2020.

[21] Texas Instruments, "LM5113 5A, 100V Half-Bridge Gate Driver for Enhancement Mode GaN FETs," p. 21, 2013.

[22] F. Krismer and J. W. Kolar, "Accurate power loss model derivation of a high-current dual active bridge converter for an automotive application," *IEEE Transactions on Industrial Electronics*, vol. 57, DOI 10.1109/TIE.2009.2025284, no. 3, pp. 881–891, 2010.

[23] G. Lakkas, "MOSFET power losses and how they affect power-supply efficiency," *Analog Applications Journal*, pp. 22–26, 2016.

[24] J. Kim, H. S. Song, and K. Nam, "Asymmetric duty control of a dual-half-bridge DC/DC converter for single-phase distributed generators," *IEEE Transactions on Power Electronics*, vol. 26, DOI 10.1109/TPEL.2010.2070877, no. 3, pp. 973–982, 2011.

[25] Efficient Power Conversion, "EPC2021 – 80 V (D-S) Enhancement Mode Power Transistor," Tech. Rep., 2019.

[26] W. Wang and M. Preindl, "Modeling and control of a dual cell link for battery-balancing auxiliary power modules," in *IEEE Applied Power Electronics Conference and Exposition (APEC)*, DOI 10.1109/APEC.2018.8341582, pp. 3340–3345, 2018.

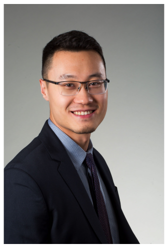

Weizhong Wang received the B.Sc. degree in electrical engineering from Harbin Institute of Technology, Weihai, Shandong, China, and the M.A.Sc. degree in electrical engineering from McMaster University, Hamilton, ON, Canada, and the Ph.D. degree in electrical engineering at Columbia University, New York, NY, USA, in 2014 and 2016, 2020, respectively. He is currently a Sr. Test Engineer at Lucid Motors, Newark, CA, USA. His research interests are battery management systems, power conversion and its magnetic designs.

Matthias Preindl (S'12-M'15-SM'18) received the B.Sc. degree in electrical engineering (*summa cum laude*) from the University of Padua, Italy, the M.Sc. degree in electrical engineering and information technology from ETH Zurich, Switzerland, and the Ph.D. degree in energy engineering from the University of Padua, in 2008, 2010, and 2014, respectively. He is currently Associate Professor of Power Electronic Systems in the Department of Electrical Engineering at Columbia University, USA. Prior to joining Columbia University in 2016, he was an R&D Engineer of Power Electronics and Drives at Leitwind AG, Italy (2010-2012), a Post Doctoral Research Associate with the McMaster Institute for Automotive Research and Technology, McMaster University, Hamilton, ON, Canada (2014-2015), and a Sessional Professor in the Department of Electrical and Computer Engineering, McMaster University (2015). He serves as the area editor of vehicular electronics and systems at the IEEE Transactions on Vehicular Technology and program chair of the 2021 IEEE Transportation Electrification Conference and Expo (ITEC). He received several awards and honors including the Horiba Awards Honorable Mention (Japan, 2019), the Futura Foundation Award (Italy, 2017), the NSF CAREER Award (USA, 2017), and he is the co-recipient of several best paper and presentation recognitions including the 2019 IEEE Transactions on Industrial Electronics best paper award.